Growth of a hard, novel CVD multilayer coating: Ti(C,N) on (Ti,Al)N on TiN

International Journal of Refractory Metals and Hard Materials 127 (2025) 106966

Contents lists available at ScienceDirect

International Journal of Refractory Metals and Hard Materials

journal homepage: www.elsevier.com/locate/IJRMHM

Growth of a hard, novel CVD multilayer coating: Ti(C,N) on (Ti,Al)N on TiN

Mohamed Ben Hassine [a,b,*], Hans-Olof Andrén [a], Anand H.S. Iyer [a], Olof Bäcke [a], Dirk Stiens [c], Wiebke Janssen [c], Johannes Kümmel [c], Mats Halvarsson [a]

[a] Dept. of Physics, Chalmers University of Technology, SE-41296 Gothenburg, Sweden
[b] Core Labs, King Abdullah University of Science and Technology (KAUST), Thuwal 23955-6900, Saudi Arabia
[c] Walter AG, Derendinger Str. 53, DE-72072 Tübingen, Germany

ARTICLE INFO

Keywords:
HRSTEM
WC-Co
Interfacial dislocations
CVD
TiCN
TiAlN

ABSTRACT

A novel chemical vapor deposition (CVD) multilayer coating intended for cutting applications was designed to achieve high wear and heat resistance during metal machining. The coating consists of three layers: a TiCN layer deposited on top of a TiAlN layer, which was grown on a layer of TiN that was deposited onto a cemented carbide substrate. The detailed microstructure of the coating was examined using a combination of electron microscope techniques. Two pyramidal surface morphologies and textures were observed, which could be related to the substrate roughness. Two growth modes were found: epitaxial growth of ⟨211⟩ oriented TiCN on <211> oriented TiAlN on <211> oriented TiN, leading to tilted TiCN pyramids at the coating surface; and epitaxial growth of ⟨111⟩ TiCN on <111> TiAlN on <111> TiN, leading to symmetrical TiCN pyramids at the coating surface.

1. Introduction

It is known that metal-cutting applications require ever-increasing cutting speeds that induce high temperatures at the tool–chip interface. TiC_xN_{1-x} is widely used as a coating material for cutting tools due to its high hardness and outstanding flank wear resistance [1]. The deposition of TiC_xN_y (from now on designated TiCN) may be done by physical vapor deposition (PVD) [2,3] or chemical vapor deposition (CVD). CVD TiCN layers are nowadays most frequently deposited by the Moderate Temperature (MT-CVD) process in the temperature range of 700–900 °C from the precursor system $TiCl_4$-CH_3CN-H_2-N_2 [4]. TiC_xN_y coatings with an increased carbon content x are expected to have improved mechanical properties, such as hardness. For this purpose, C_2H_4 [5,6] or C_2H_6 [7] have been used as additional or alternative precursors to the $TiCl_4$-CH_3CN-H_2(—N_2) precursor system. Considerable effort has been devoted to improve the cutting performance of MT-CVD TiCN coatings by adding $ZrCl_4$ [8], BCl_3 [9] and CO [10,11] to the precursor system to refine the structure and improve the grain morphology and orientation.

One way to increase the metal-cutting performance of hard coatings is to adjust the microstructure of the grains. TiCN coatings have been reported to have different crystallographic textures. Larsson and Ruppi have studied the microstructure and properties of TiCN coatings deposited on cutting tool substrates using MT-CVD and exhibiting a ⟨211⟩ texture and columnar grain morphology [12]. They found that MT-CVD TiCN coatings have better edge chipping resistance, but worse crater wear resistance, compared to the High Temperature (HT) CVD TiCN coatings [12]. Von Fieandt et al. studied the formation of texture in MT-CVD TiCN coatings on sapphire substrates [13,14]. They found that the <111> textured TiCN had a higher hardness than <211> textured TiCN [13]. The authors explained the hardness increase of <111> textured coatings compared to <211> by a higher degree of epitaxy with the {0001} oriented sapphire substrate. The change in orientation also caused a change in the microstructure and morphology to a larger grain size than in the <211> oriented coating. Recently, Qiu et al. studied the influence of crystallographic texture of MT-CVD TiCN coating on plastic deformation in machining [15]. The results of simulations by Schmid factor analysis were compared to the wear generated on the rake face of cutting inserts by short longitudinal turning tests for coatings with {100} and {211} growth textures. It was found that the observed plastic deformation is consistent with simulation results for the {110}⟨110⟩ slip systems [15].

Another way to increase the performance of hard coatings is to combine layers of different materials creating multilayered coatings. The most frequently used multilayer sequences include TiN, TiCN, and Al_2O_3 [16,17]. However, the large lattice mismatch between adjacent layers could cause poor adhesion due to a high amount of strain over the interfaces.

* Corresponding author at: Dept. of Physics, Chalmers University of Technology, SE-41296 Gothenburg, Sweden.
E-mail address: mohamed.benhassine@kaust.edu.sa (M. Ben Hassine).

https://doi.org/10.1016/j.ijrmhm.2024.106966
Received 13 August 2024; Received in revised form 14 November 2024; Accepted 14 November 2024
Available online 17 November 2024

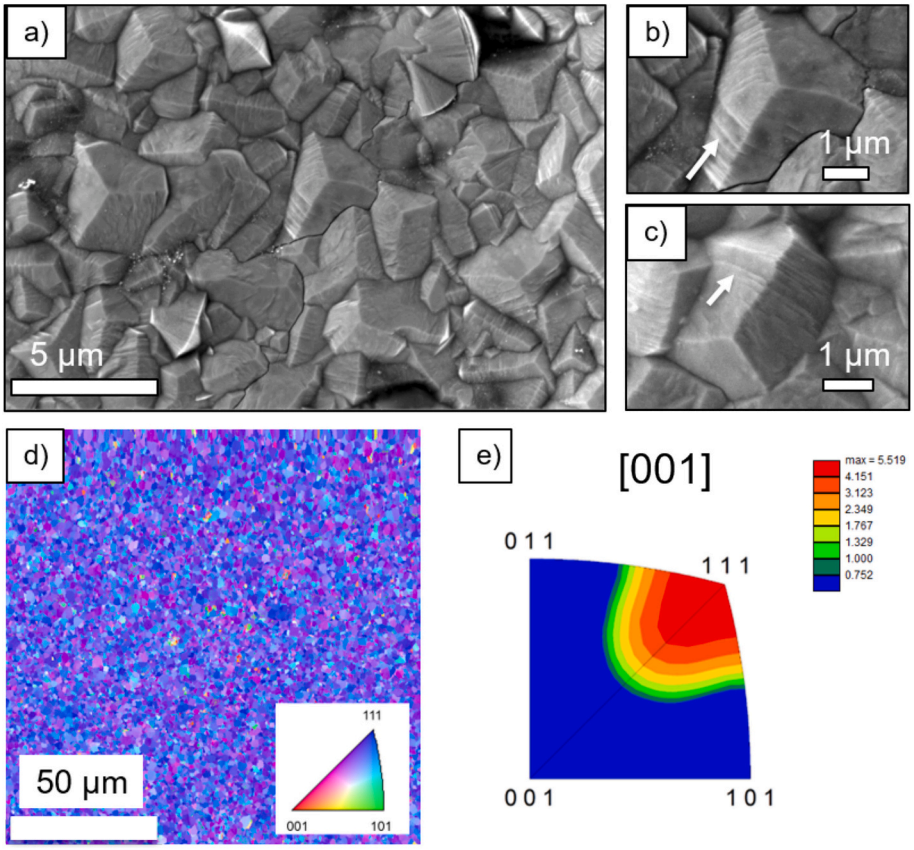

Fig. 1. a) SEM micrograph of the top coating surface showing a pyramid morphology of TiCN grains. b and c) High magnification SEM images of the pyramid grain, the arrows indicate surface steps on the TiCN pyramids. d) IPF map in the Z (surface normal) direction of the TiCN layer; the insert represents the color legend for the IPF map. e) IPF contour plot for the Z direction.

In the present work, we investigate a novel multilayered wear-resistant coating structure, comprising an inner CVD coating layer of titanium aluminum nitride, $Ti_{1-u}Al_uN_v$ (from now on designated TiAlN) with a {111} fiber texture, followed by a second MT-CVD TiCN coating layer. A thin titanium nitride (TiN) layer is deposited directly onto the substrate in order to enhance the coating adhesion, i.e. in total three layers were deposited. TiAlN is a well-established material for cutting tool applications exhibiting high hardness and excellent oxidation resistance. Recent developments have made it possible to use CVD to deposit TiAlN coatings with an Al/Al + Ti ratio of around 0.9, which is accompanied by an extensive hardening effect [18]. A nanolamellar structure with alternating Ti/Al concentration ratio has been observed for CVD TiAlN coatings [19].

We study the multilayer structure using different electron microscope techniques in order to understand the growth mechanisms of the coating. The relation between the substrate morphologies and the coating textures is described in detail. Also, this investigation explains how the multilayer systems accommodates the strain generated by the difference in lattice parameters between the different layers.

2. Experiments

2.1. Sample preparation

This study concerns a coated cutting tool consisting of a substrate of cemented carbide and a multi-layered wear-resistant coating having a total coating thickness of about 12 µm, comprising three refractory coating layers deposited by CVD or MT-CVD in an industrial-scale reactor. The first coating layer is TiN, deposited onto a polished cemented carbide substrate at a temperature of 850 °C and a pressure of 15 kPa. The second layer consists of $Ti_{1-u}Al_uN_v$ with $0.7 < u \leq 0.9$, and is deposited by CVD at a reaction temperature of 700 °C. The third coating layer consists of titanium carbonitride TiCN and is deposited at a reaction temperature of 850 °C.

2.2. Electron microscopy characterization

The morphology of the samples was studied by scanning electron microscopy (SEM) in an FEI Versa 3D FIB/SEM (Focused Ion Beam/Scanning Electron Microscope) equipped with a field emission gun (FEG). SEM images were recorded at an accelerating voltage of 5 kV. In addition, thin-foil lamellae were obtained using the same FIB/SEM. Electron backscatter diffraction (EBSD) was performed on the polished sample surface in order to obtain an overview of the grain orientations with respect to the growth direction of the film. EBSD was made using a Zeiss Crossbeam 540 / EDAX DigiView 5 system operated at 15 kV and 4.8 nA over an area of approximately 150 µm × 150 µm using a step size of 75 nm. Transmission Kikuchi diffraction (TKD) was performed using a TESCAN GAIA3 FIB/SEM at 30 kV acceleration voltage and a 30 nm step size on an electron transparent thin-foil lamella.

Transmission electron microscopy (TEM) and scanning transmission electron microscopy (STEM) imaging were obtained with a Cs-corrected FEI Titan 80–300 microscope equipped with a FEG source and a monochromator, operated at 300 kV. STEM images were collected using Bright Field (BF) and High Angle Annular Dark Field (HAADF) detectors. STEM images were acquired with a probe current of ~100 pA and a convergence semi-angle of 20 mrad and processed using the TEM Imaging and Analysis (TIA) software from FEI. Compositional analyses of grains were conducted in STEM mode with an energy-dispersive X-ray spectrometer (EDX) equipped with an Oxford INCA thin-window Si(Li)

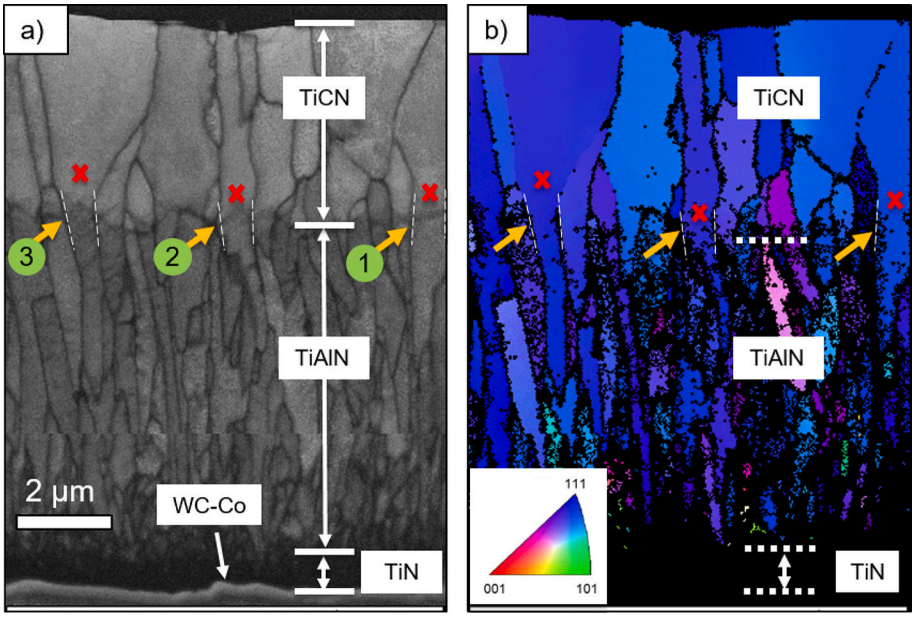

Fig. 2. a) TKD band contrast map of the coating cross-section showing the columnar morphology of the TiAlN and TiCN grains. The yellow arrows indicate an epitaxial relationship between the TiAlN and TiCN grains. b) IPF map in the Z (surface normal) direction, in which the yellow arrows indicate the same grains as marked in Fig. 2a. The insert represents the color legend for the IPF map. (For interpretation of the references to color in this figure legend, the reader is referred to the web version of this article.)

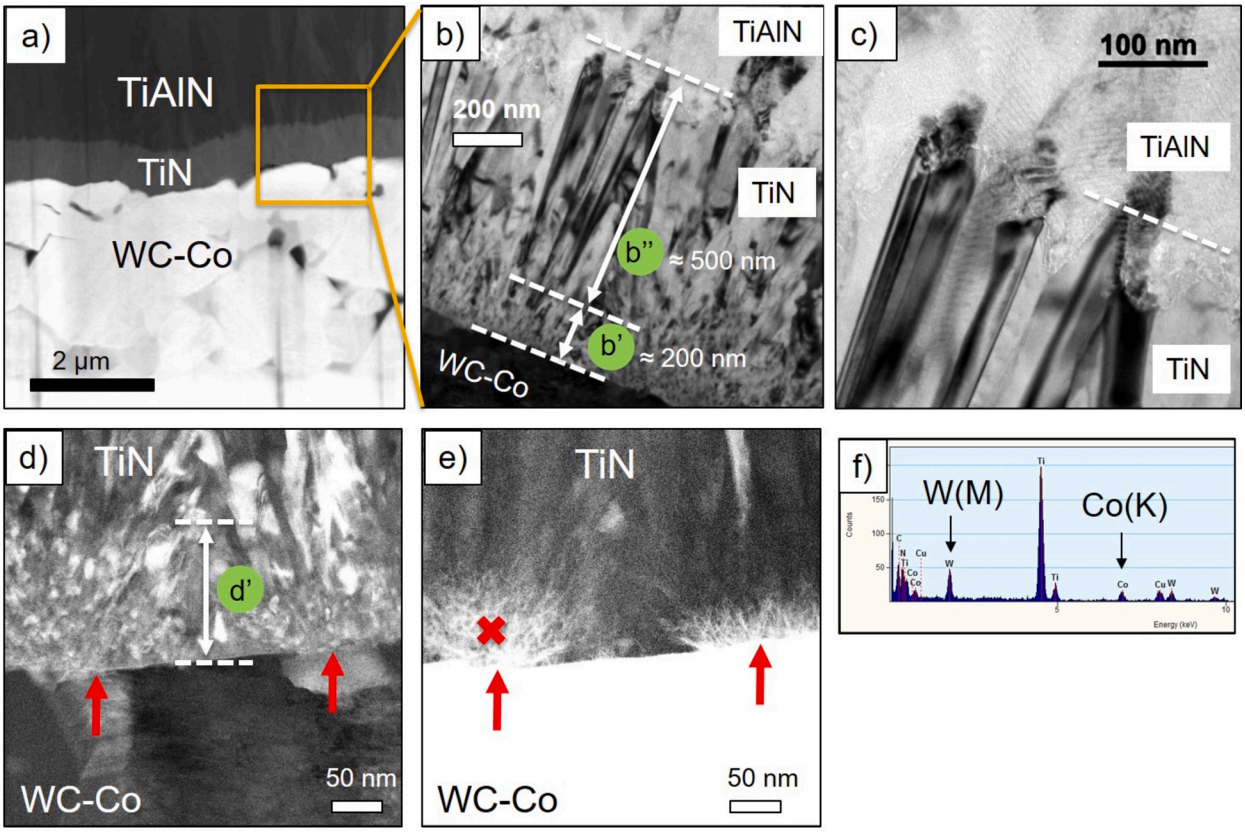

Fig. 3. a) HAADF-STEM image of the interface between the substrate and the coating. b-c) TEM images of TiN forming two sub-layers: b' formed by small equiaxed grains and b" formed by columnar grains. d-e) STEM images collected by the BF and HAADF detectors, respectively, showing the diffusion of W and Co from the substrate binder phase into TiN. f) EDX spectrum collected from the X-marked position in Fig. 3e.

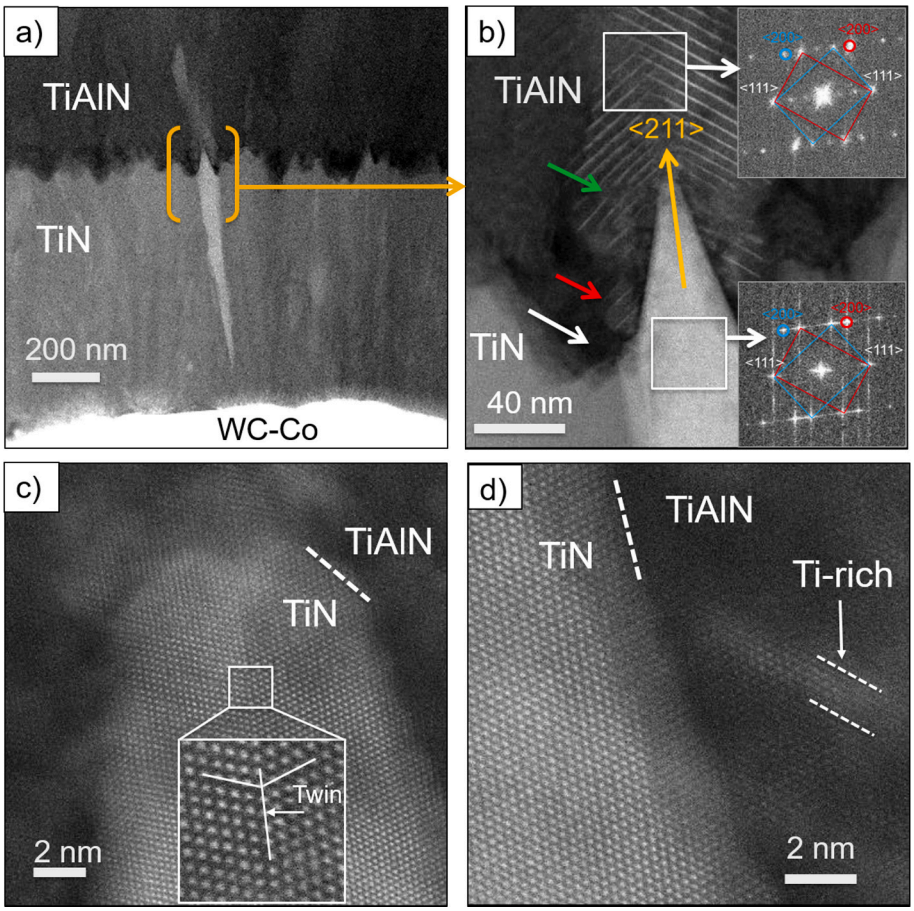

Fig. 4. a-e) HAADF-STEM images of the interface between TiN and TiAlN above the substrate surface being parallel to the coating surface. a) Needle-shaped morphology of the TiN grains. b) Higher magnification of the area marked by the bracket in Fig. 4a showing the epitaxial growth of two grains of TiAlN on top of a twinned TiN grain. The inserts in Fig. 4b present the FFTs calculated from TiAlN and TiN, respectively. c) HAADF-STEM image of a TiN grain showing a twinned structure. d) High magnification HAADF-STEM image of the TiAlN and TiN interface.

detector and controlled by the TIA software. Image processing was made with the DigitalMicrograph software from Gatan.

3. Results and discussion

3.1. Overview of the coating top surface

Fig. 1a shows an SEM image collected from the top coating surface of the investigated insert. The overview highlights a pyramid shape of TiCN grains with a three-fold symmetry and a distribution of grain sizes varying between 0.5 μm and 4 μm. The high magnification SEM images show that some TiCN grains have symmetric (Fig. 1b) and others tilted (Fig. 1c) pyramidal surface morphologies. Grains with pyramids, symmetric and tilted morphologies, all have sharp edges with a curvature which follows the steps on the facets. Some facets exhibit distinct steps and the estimated distance between the facet steps (obtained from the SEM micrographs) is in the range of ~10–30 nm (arrows in Fig. 1b and c). To our knowledge TiCN grains with a three-fold symmetry have not been observed before; note that the formation of pyramids with three-fold symmetry is associated with the growth direction <111> for TiAlN coatings [19–21].

EBSD data was collected from the TiCN layer from which the surface asperities were polished away to a mirror finish in order to identify the crystallographic texture. The obtained inverse pole figure (IPF) map and the corresponding color legend are shown in Fig. 1d. Contour plots made in the Z (surface normal) direction for the inverse pole figures show a high uniform density close to the <111> direction, implying that most grains are oriented close to this direction (Fig. 1e).

3.2. Overview of the coating cross-section

TKD data were collected from FIB lamellae in order to get information about the crystallographic texture along the coating cross-section. The band contrast map highlights a columnar morphology of the TiAlN layer in which the grains are slightly tilted versus the substrate normal (Fig. 2a). The TiAlN grain widths are around 0.5 μm and the heights several microns, around 7.5 μm; often the grains extend almost all the way through the layer. Above the TiAlN layer, the grains of TiCN grow with a size distribution between 500 nm and 3 μm. The thickness of the TiCN layer is about 4 μm. For the bottom TiN layer, the thickness measured by TEM (below) was found to be around 700 nm. Because of the small grain size of TiN, this layer is not clearly identified in the band contrast image (Fig. 2a). The microstructure details of TiN layer will be given in paragraph 3.4 using TEM techniques.

The IPF map for the surface normal direction and the corresponding color legend are shown in Fig. 2b. The map shows a clear texture for both layers, close to the <111> direction. In addition, the band contrast image highlights epitaxial growth between the grains of TiAlN and TiCN, as shown by the continuous growth of the TiCN grains (yellow arrows in Fig. 2a and b).

3.3. Interface between the WC-Co substrate and TiN layer

Fig. 3a shows a HAADF-STEM image of the interface between the

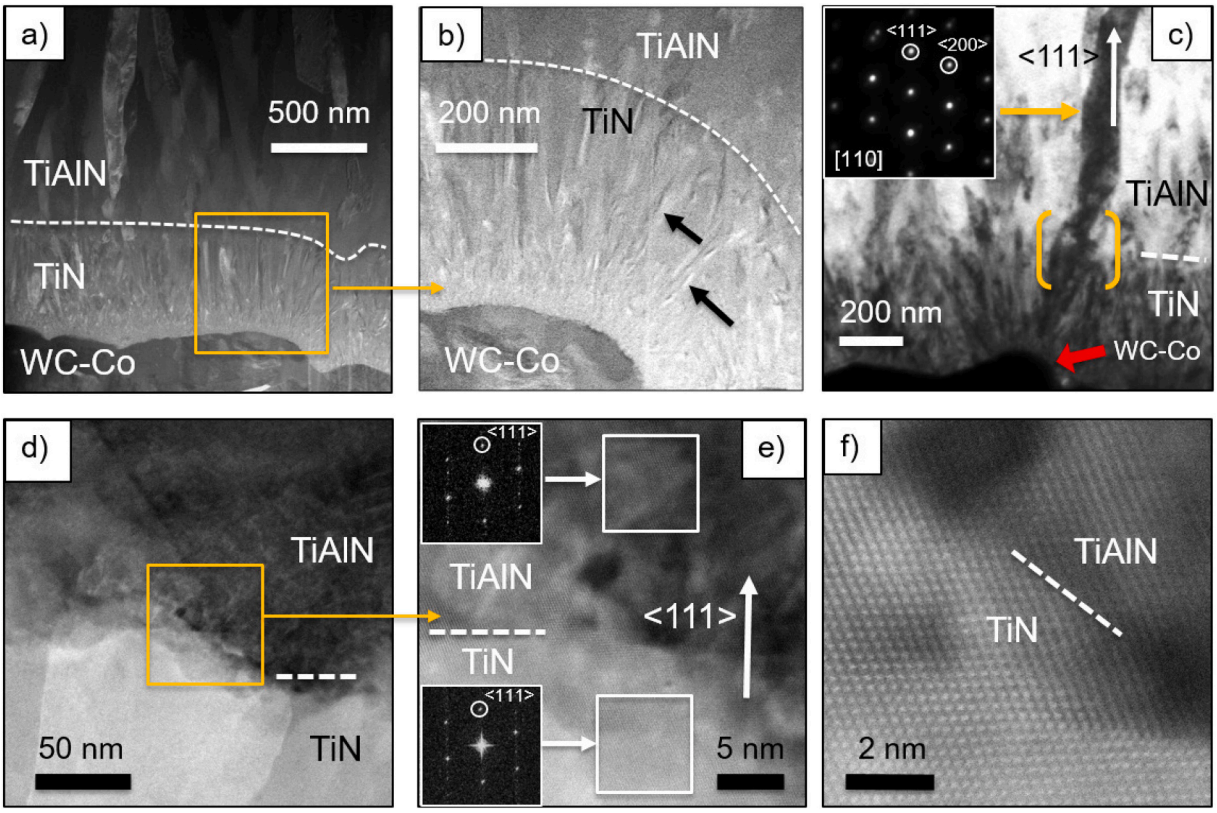

Fig. 5. a-b) BF-STEM images of the bottom of the coating above an inclined substrate surface. c) TEM image of the interface between TiN and TiAlN, the brackets indicate a TiN grain growing on top of an inclined WC grain. The dark contrast reveals a crystallographic relationship between the two layers (Fig. 5c and d). The insert in Fig. 5c shows the SAED corresponding to the marked TiAlN grain indicating a growth along the <111> direction. d-f) HAADF-STEM images of the grains marked by brackets in Fig. 5c. The inserts in Fig. 5e show the calculated FFTs from the STEM image highlighting the epitaxy between TiN and TiAlN.

substrate and the coating. The overview shows the surface roughness of the WC-Co substrate and the size of the WC grains that varies between 0.5 μm and 2 μm. Fig. 3b–e present BF-TEM and STEM images from different areas inside the square in Fig. 3a. Two different morphologies can be distinguished in the TiN layer. At the bottom, the TiN layer is formed by small equiaxed grains (Fig. 3d'), while at the top (Fig. 3b") TiN has a columnar morphology, with grain heights of 500 nm and widths around 70 nm (Fig. 3c).

In order to get more details about the equiaxed (b') layer, STEM imaging was performed at the interface between WC-Co and TiN. Fig. 3d and e present two STEM images collected using the BF and HAADF detectors, respectively, from the same area. In Fig. 3d, the layer d' represent a magnification of the layer b' of Fig. 3b, which is formed by a fine granular structure with a grain size of about 10 to 50 nm. The red arrows indicate the (Co-rich) binder phase areas of the cemented carbide substrate; the darker areas are WC grains (Fig. 3d and e). Fig. 3e shows several bright lines extending from the binder phase areas in WC-Co to approximately 100 nm into the TiN layer. As the HAADF image gives *Z*-contrast, these lines correspond to heavy elements, Co and/or W (Fig. 3e). Supplementary EDX analyses were carried out to check the composition of these bright lines. The EDX spectrum collected from the bright lines reveals a significant signal of both W and Co (Fig. 3f). Quantification of the metal content indicated an approximate composition of $(Ti_{0.90}W_{0.04}Co_{0.06})N$ if it is assumed that no C in-diffusion occurs and that the content of nitrogen is taken to be stoichiometric (the contents of C and N were not measured). Carbon was not measured, but probably present from in-diffusion from the substrate. It can thus be noticed that the W and Co come from the Co-rich and W-containing binder phase of WC-Co that diffuse up into the TiN layer following the grain boundaries of TiN, giving the white lines in the HAADF-STEM image of Fig. 3e.

3.4. Interface between TiN and TiAlN

As the substrate surface has a certain roughness, in some areas the WC grains have a surface that is parallel to the coating surface (the macroscopic surface of the sample), while in other areas their surfaces are inclined to the coating surface. Two different TiN layer growths were found on these two substrate surface orientations, resulting in <211> and ⟨111⟩ growth of TiAlN on parallel and inclined surfaces, respectively. These two cases are described in 3.4.1 and 3.4.2.

3.4.1. Locally horizontal substrate surface: <211> epitaxial growth of TiAlN on top of twinned TiN

Fig. 4a-e show HAADF-STEM images from the bottom of the coating, with a substrate locally horizontal surface, i.e. parallel to the sample surface, and needle-shaped TiN grains. Fig. 4b-e present higher magnification micrographs of the area marked by the brackets in Fig. 4a. For these images, the difference in contrast represents the difference in the mean atomic weight of the elements constituting the coatings [22]. Therefore, the bright nanolamellae observed in Fig. 4b are relatively rich in Ti, since Ti is heavier than Al and N.

The inserts in Fig. 4b show the calculated Fast Fourier transforms (FFTs) from the HAADF-high resolution STEM (HRSTEM) images of TiAlN and TiN, indicating a face-centered cubic (FCC) structure for both materials. All reflections could be indexed using the space group $Fm\bar{3}m$ and cell parameters: $a = 4.08$ Å (for TiAlN) and $a = 4.24$ Å (for TiN). As indicated in Fig. 4b, the TiN needle growth is found to be along <211> direction, and slightly inclined to the normal of the substrate.

For TiAlN, the FFT is formed by the superposition of two diffraction patterns, corresponding to two grains with different crystallographic orientations (insert in Fig. 4b). Indeed, the periodic Ti-rich lamellae have two different orientations to the left and right of the TiN needle,

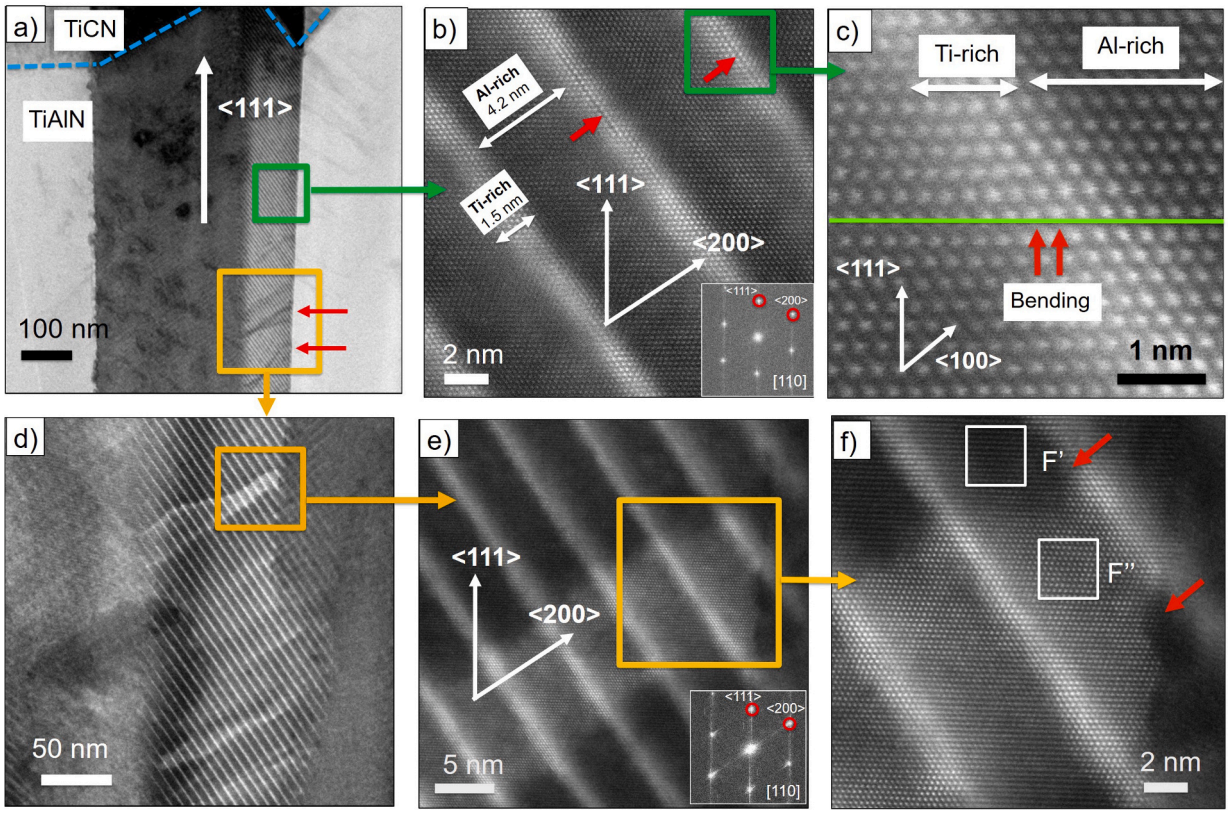

Fig. 6. a) BF-STEM image collected from the upper part of the TiAlN layer: the green rectangle shows a homogenous region. b-c) HAADF-STEM images of the area marked by green square in a) highlighting periodic bright (Ti-rich) and dark (Al-rich) lamellae. Dark lines are observed inside the Ti-rich lamellae (red arrows). c) HAADF-STEM image showing bending of an atomic plane across Al-rich and Ti-rich lamellae. e-f) HAADF-STEM images: high magnification of the dislocations area. In F″ (bright area) the atomic columns are very well defined, while in F′ (dark area) the atomic columns have a weaker contrast due to dislocation-induced distortions of the lattice. (For interpretation of the references to color in this figure legend, the reader is referred to the web version of this article.)

indicating the presence of two TiAlN grains (Fig. 4b). The calculated FFT from the HRSTEM image of TiN also exhibits two overlapping diffraction patterns (insert in Fig. 4b). In this case, the two patterns correspond to a twinned <211> – oriented TiN grain. The HAADF-HRSTEM image collected from TiN (Fig. 4c) gives a clear picture of the twinned structure in the TiN grain. Moreover, the two FFT patterns, corresponding to TiAlN and TiN, are similar, which means that both materials have the same crystallographic structure and orientation, indicating an epitaxial cube-on-cube growth of TiAlN on top of TiN.

Similar results were reported in our earlier work, where two grains of TiAlN grown epitaxially on top of one twinned TiN grain, which led to the so-called "two-wings" structure [19]. Here, a similar growth mechanism is identified. The difference is that the TiN grain needles are sharper and the <211> axis is slightly tilted away from the vertical direction. Moreover, many defects are present at the interface of both materials because of the cell parameter mismatch between TiN and TiAlN. Discontinuities of the Ti-rich lamellae are identified at the interface (green arrow in Fig. 4b). Also, a sort of TiAlN nanograins is observed at the interface (red arrow in Fig. 4b). In some areas, a dark area is observed at the interface TiN and TiAlN (white arrow Fig. 4b). Since the HAADF detector gives *Z*-contrast, these areas should be rich in Al (and N), and are thought to be AlN regions since a similar nanograin in a TiN/TiAlN interface has been found before, and was found to be cubic and with an Al/(Al + Ti) ratio of 0.96 [19]. Fig. 4d shows the TiN – TiAlN interface in higher magnification.

3.4.2. *Locally inclined substrate surface: <111> epitaxial growth of TiAlN on un-twinned TiN*

Fig. 5a-b show BF-STEM images from the bottom of the coating, with a locally inclined substrate surface. The surface morphology of the substrate indicates WC grains having different shapes and sizes. On top of these surface areas, the grains of TiN grow inclined, perpendicular to the local surface, following the morphology of the substrate. The tilted grains are marked by arrows in Fig. 5b. Note that the TiN layer has the same grain morphology as in the parallel surface case (described above) with equiaxed grains close to the surface and columnar grains further up.

Fig. 5c shows a TEM image at the interface between the TiN and TiAlN layers. TiN grains are observed on top of a curved WC grain (marked by a red arrow in Fig. 5c). The TiN grains start to grow on the substrate perpendicularly to the surface. The insert in Fig. 5c shows a Selected Area Electron Diffraction (SAED) pattern collected from the dark TiAlN grain, revealing an FCC structure with local grain growth along <211>, leading to an overall <111> texture, as the growth direction is inclined with respect to the substrate normal. The dark contrast of Fig. 5c indicates a crystallographic relationship between the grains of TiN and TiAlN. Fig. 5d-f are HAADF-STEM images of the area marked by brackets in Fig. 5c. The inserts in Fig. 5e show calculated FFTs from TiAlN and TiN materials. Since the FFT patterns are similar, epitaxial growth is identified. Further evidence of the epitaxial growth is given by the continuous rows of atomic columns between the materials (Fig. 5f).

In conclusion, the inclined surface of the WC-Co substrate induces the formation of tilted TiN grains growing with their <111> directions fairly perpendicular to the coating surface. On top of the tilted TiN grains, TiAlN grows epitaxially along the same direction, leading to a <111> texture also for TiAlN.

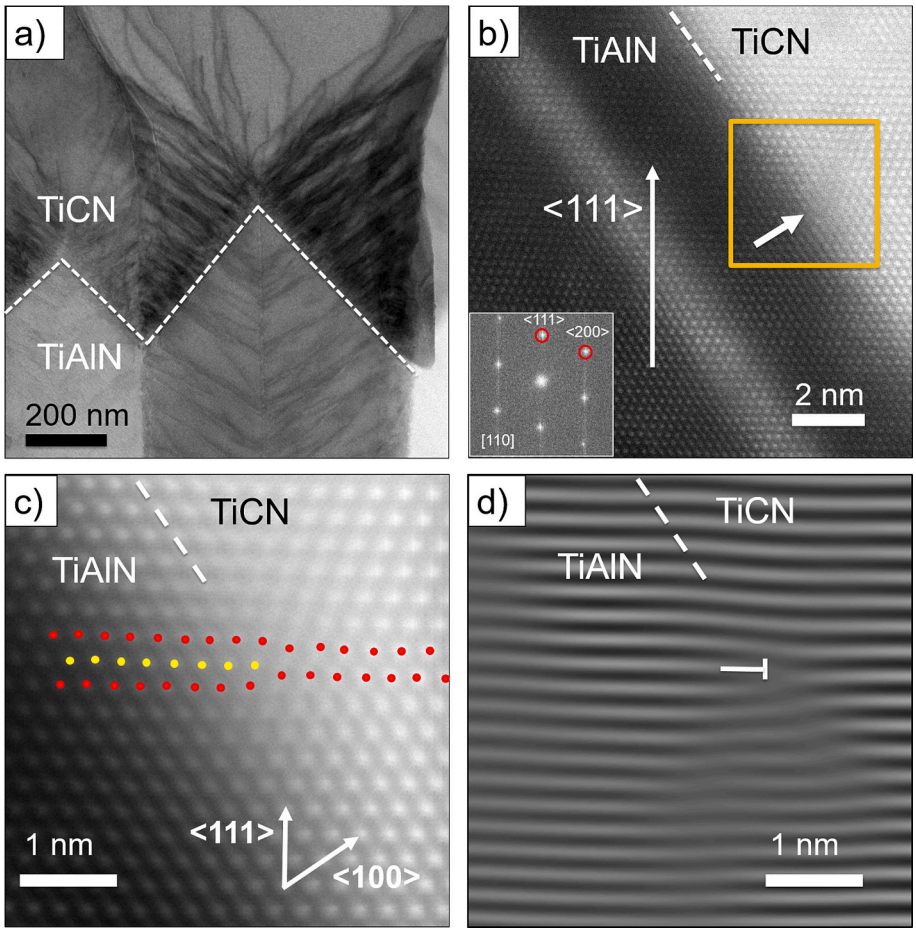

Fig. 7. a) BF-STEM image of the TiAlN and TiCN interface showing several dislocations arising from the TiAlN pyramid facets. These dislocations then extend to the edges of the TiCN grains. b) HAADF-STEM image showing epitaxy between TiAlN and TiCN. c) IFFT indicating the presence of an additional half plane in TiAlN material. d) IFFT image calculated by masking the (111) reflections in the FFT of Fig. 7c.

3.5. TiAlN microstructure

Fig. 6a shows a BF-STEM image collected from the upper part of the TiAlN layer. The overview reveals that the grains do not appear in the same way; in some regions the material looks homogeneous (green rectangle), while in other regions several dark lines are visible inside the grain to the grain boundary (marked by red arrows in Fig. 6a). Fig. 6b is a HAADF-HRSTEM image of the homogenous region, periodic nano-lamellae with a thickness of approximately 4.2 nm for dark lamellae (Al-rich) and 1.5 nm for bright lamellae (Ti-rich) are visible. The insert represents the calculated FFT illustrating that both phases (Al-rich and Ti-rich) exhibit the FCC structure and a $< 111 >$ growth along the insert surface normal. A closer examination of the Ti-rich lamellae reveals the presence of dark lines along the lamellae (marked by red arrows in Fig. 6b). For better visualization, the high magnification HAADF-STEM micrograph of the area marked by a rectangle in Fig. 6b is presented in Fig. 6c. The drawn straight line highlights a bending of atomic planes at the interface between Al-rich and Ti-rich lamellae. This bending probably stems from the lattice parameter difference between Al-rich and Ti-rich lamellae. Still, the interface is coherent, which means that the Ti-rich layer with the larger lattice parameter is compressed along the interface and therefore expands in the growth direction. This expansion along [100] gives a tilt of the (111) planes in the Ti-rich lamella, and a tilting back to the same orientation in the adjoining Al-rich lamella.

Fig. 6d-f show HAADF-STEM images of the area marked by the yellow rectangle in Fig. 6a. The FFT in Fig. 6e again indicates an FCC cubic structure of TiAlN material. The bright areas observed in Fig. 6d-f are rich in Ti. The high magnification HAADF-STEM image (Fig. 6f) gives the microstructure details of this area: in the bright region marked by F″, the atomic columns are very well-defined providing a very well-defined lattice. However, in the dark region marked by F′, the atomic columns are less pronounced. We believe that two dislocations are going through the lattice TiAlN (marked by red arrows in Fig. 6f). Each dislocation bends the lattice somewhat. The bright contrast between the dislocations is due to a perfect beam-crystal alignment, as seen in (Fig. 6f-F″), and the dark contrast on both sides is due to the bending of the lattice destroying the alignment, reducing the atomic column contrast (Fig. 6f-F′). This means that the contrast in Fig. 6e-f is not solely *Z*-contrast, but some diffraction contrast (sensitivity to orientation) remains in the micrographs, due to using a rather long camera length during image acquisition. The two dislocations are probably threading dislocations, generated at the interface between the two TiAlN domains and growing essentially perpendicular to the (100) growth facet. Several such dislocations can be seen in Fig. 6a and d. The cause of lamella formation is explained in reference [20]. It shows that a rotational precursor gas supply induces an oscillatory surface reaction, leading to the formation of nanolamellae architectures.

3.6. Interfacial dislocations between TiAlN and TiCN

The difference in lattice parameter between TiCN (4.33 Å) and TiAlN (4.08 Å) gives a lattice mismatch of 6 %. Such a mismatch usually leads to a high interfacial energy and the formation of misfit dislocations. Fig. 7a shows a low-magnification BF-STEM image of the interface between the TiCN and TiAlN layers. Several dislocations were observed as dark lines in the TiCN material starting at the TiCN/TiAlN interface. The

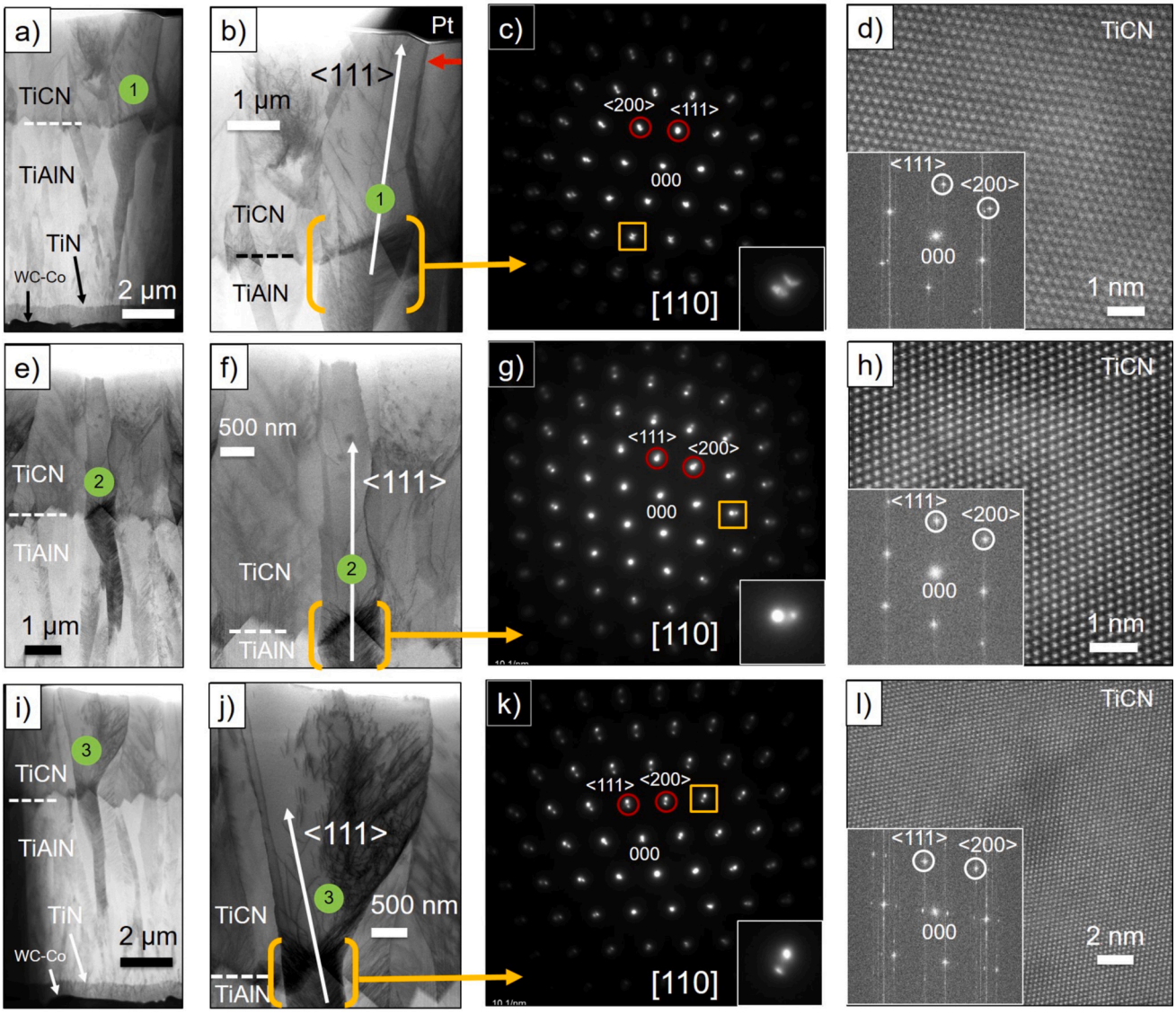

Fig. 8. a), e) and i): BF-STEM images of the grains marked 1, 2 and 3 in Fig. 2, respectively. b), f), and j) show the BF-STEM images of the upper areas of the grains 1, 2 and 3 respectively, highlighting several dislocations at the TiAlN/TiCN interface. c), g), and k): SAED patterns collected at the TiAlN/TiCN interface, showing that both materials grow along <111>. The patterns reveal an epitaxial growth of TiCN on TiAlN. d), h), and l): HAADF-STEM images of TiCN; the inserts are the corresponding FFTs.

dislocations propagate almost perpendicularly from the TiAlN pyramid facets towards the edges of the TiCN grains. Few dislocations extend to the top of the coating. These dislocations are probably all threading dislocations. These threading dislocations are only found in the bottom part of TiCN grains, generated at the phase boundary, whereas the whole TiAlN grains are filled with other threading dislocations, generated either at the center of the TiAlN grains, probably on local thin AlN regions or at Ti-rich and Al-rich lamellae interfaces.

Fig. 7b shows a high-resolution HAADF-STEM micrograph of the TiCN-TiAlN interface. For TiCN, the atomic columns of Ti are expected to appear significantly brighter than both C and N columns, which are not heavy enough to produce any contrast and, thus, are basically not visible. Therefore, the *Z*-contrast image highlights a material with very regular stacking of Ti planes. The insert represents the calculated FFT, indicating an FCC structure of both materials (TiCN, TiAlN), a macroscopic growth along the <111> direction and {100} lamellae surfaces. The continuous lattice between TiAlN and TiCN gives additional evidence for the same type of crystal structure in the layers, and indicates a cube-on-cube epitaxy. However, the image exhibits a loss of the atomic column contrast in an area at the TiCN and TiAlN interface (arrow in Fig. 7b). For better visualization, the HAADF-STEM images were processed by first masking spots in the FFT of the original image and then using an inverse FFT (IFFT) to get back real-space data. Fig. 7c shows a magnification of the area marked by a rectangle in Fig. 7b. The colored dots designate the positions of the atomic columns. A closer examination highlights the presence of an additional half plane in TiAlN close to the interface with TiCN (yellow dots). Fig. 7d shows the IFFT image obtained by selecting only the (111) reflections of the FFT from the same area of Fig. 7c, providing clear evidence of an interfacial dislocation. Evidently, the mismatch in lattice parameter results in the formation of misfit dislocations at the interface typical of a semi-coherent interface.

3.7. <111> epitaxial growth of TiCN on top of TiAlN

Fig. 8a, e, and i show BF-STEM images of the grains marked by 1, 2 and 3 in Fig. 2, respectively. The above overview indicated the presence of some tilted and some straight grains in the multilayer coating: In grain number 1 the <111> direction is tilted to the right, in grain 2 it is

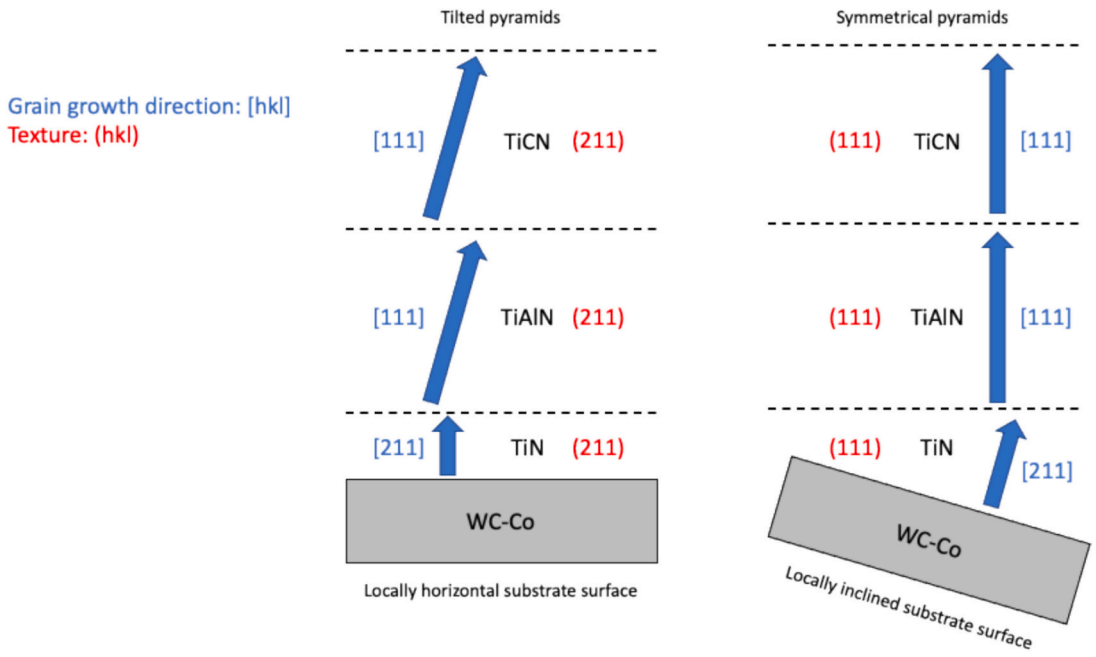

Fig. 9. Schematic drawings describing the growth of the multilayer coating TiN/TiAlN/TiCN, with either a locally horizontal substrate surface, leading to a tilted pyramidal surface morphology, or a locally inclined substrate surface, leading to a symmetrical pyramidal surface morphology. The grain growth directions for the 3 layers are schematically shown by blue arrows and [hkl] directions, and the layer textures (hkl) are given in red. (For interpretation of the references to color in this figure legend, the reader is referred to the web version of this article.)

straight, and in grain 3 it is tilted to the left. Fig. 8b, f, and j show BF-STEM images of the upper parts of grains 1, 2 and 3, respectively. As outlined above, the dark lines represent dislocations inside TiCN grains starting at the interface with TiAlN. Only a few dislocations spread to the top surface of the TiCN grains.

SAED patterns were collected from regions at the TiCN and TiAlN interfaces, marked by brackets (Fig. 8c, g and k). The inserts show a magnification of the reflections marked by the yellow rectangles in Fig. 8c, g and k. The patterns reveal the presence of epitaxy between grains with different cell parameters. The reflections could be indexed using the following cell data: $Fm\bar{3}m$; a = 4.33 Å (for TiCN) and a = 4.08 Å (for TiAlN). Fig. 8d, h and l show HAADF-STEM images collected from grains 1, 2, and 3, respectively, exhibiting a well-crystallized TiCN material. The inserts in Fig. 8d, h and l show the FFTs from the HAADF-STEM images, consistent with the SAED results. The arrows drawn in Fig. 8b, f and j are giving the <111> directions based on the FFT of Fig. 8d, h, and l.

Fig. 8b shows that the top part of the FIB lamella was partly lost by the ion beam milling. In the area where the deposited platinum layer survived, the surface of the TiCN grain was protected from the ion beam sputtering. This top grain shape has a pyramid morphology (red arrow in Fig. 8b). The calculated FFT reveals that the <111> axis is common for the top pyramid grain of TiCN and the underlying TiAlN grain. Therefore, the pyramid morphology previously observed on the coating surface using SEM imaging (Fig. 1) is explained by the epitaxial growth of TiCN on the top of TiAlN along the <111> direction, with three {001} facets. Various surface morphologies have been reported for MT-CVD TiCN coatings depending on the crystallographic texture: facets with two-fold symmetry for {211} or {110} oriented grains [15,23], star-shaped crystals with five {111} twin boundaries along ⟨110⟩ [24], or facets with four-fold symmetry for {100} oriented grains [15]. However, in this investigation, the TiCN grains have a three-fold symmetry. To our knowledge, this is the first time that a pyramid morphology of TiCN grains, growing along <111> direction perpendicular to the substrate, is identified for CVD TiCN.

3.8. General growth description

Based on the above-described results, a general description of how the growth of the different layers occur and lead to a difference in surface morphology can be made. Schematic drawings describing the growth of the multilayer coating TiN/TiAlN/TiCN is found in Fig. 9. For a locally horizontal substrate surface, this results in a (211) textured growth of TiAlN on the TiN layer (Fig. 4). The TiAlN then grows epitaxially, with grain growth oriented along [111] [19], slightly tilted relative to the coating normal. This growth pattern has previously been described as a "two-wing model," in which two TiAlN grains inclined to the left or right resemble two wings [19]. Epitaxial cube-on-cube growth of TiCN on the underlying TiAlN (Figs. 2 and 8) leads to TiCN crystals with a tilted pyramidal surface morphology (Fig. 1). All three layers have a (211) texture.

For a locally inclined substrate surface, this leads to (111) textured growth (Fig. 6) of TiAlN on TiN (Fig. 5). Epitaxial growth (Figs. 2 and 8) of TiCN on TiAlN leads to all layers in this case having (111)-textures with a symmetrical pyramidal surface morphology (Fig. 1).

4. Conclusions

In this work, a CVD multilayer coating, consisting of TiN (lower), TiAlN (middle) and TiCN (upper) layers grown on a WC-Co substrate, is investigated. The growth directions, grain morphologies, microstructure and composition were studied by analytical scanning transmission electron microscopy. The main results and conclusions of the study are summarized as follows:

- The surface of the substrate has a certain roughness. The grains in the inner TiN layer grow in different directions, following the local orientation of the substrate surface. W and Co from the binder phase in the substrate diffuse into the TiN layer along its grain boundaries.
- The TiN, TiAlN and TiCN grains all have columnar morphologies, where TiAlN grows with a cube-on-cube epitaxial relationship on the TiN layer, and similarly TiCN grows epitaxially on TiAlN with a cube-on-cube orientation relationship. In this way the texture of the TiN

layer is maintained vertically for the three coating layers. Two local textures were observed, (111) and (211).

- The TiN layer contains an inner region (thickness about 200 nm) of small grains followed by an outer region (thickness about 500 nm) of columnar grains, often exhibiting twins.
- Several defects were identified at the interface between TiN and TiAlN, such as discontinuities of the nano-lamellae.
- The TiAlN grains contain three growth domains, giving three {001} facets. An internal nano-lamella structure with alternating Ti-rich and Al-rich domains is present within the TiAlN grains.
- Threading dislocations start from the TiAlN grain centers, and spread to the grain edges. The dislocations induce distortions of the lattice and the nano-lamellae. A bending of atomic planes was identified between Al-rich and Ti-rich lamellae due to local strains at the interfaces.
- The strain generated by the lattice misfit of TiCN and TiAlN is relaxed by interfacial dislocations. For TiCN, threading dislocations arise from the pyramid facets of the underlying TiAlN grains and spread to the edges of the TiCN grains.
- The TiCN grains at the top surface have pyramidal shapes with two surface morphologies, symmetric and tilted pyramids, related to a < 111> grain growth either parallel or inclined to the coating normal, corresponding to a (111) or (211) local texture.

In summary, a growth model could be proposed to explain the observed variations in grain orientations and surface morphologies for the multilayer coating.

CRediT authorship contribution statement

Mohamed Ben Hassine: Writing – review & editing, Writing – original draft, Visualization, Validation, Investigation, Formal analysis, Data curation. **Hans-Olof Andrén:** Writing – review & editing, Visualization, Validation, Supervision, Methodology. **Anand H.S. Iyer:** Formal analysis, Data curation. **Olof Bäcke:** Writing – review & editing, Visualization, Validation, Methodology, Investigation, Formal analysis. **Dirk Stiens:** Writing – review & editing, Visualization, Validation, Supervision, Resources, Project administration, Methodology, Funding acquisition, Conceptualization. **Wiebke Janssen:** Visualization, Investigation. **Johannes Kümmel:** Writing – review & editing, Visualization, Validation, Methodology, Investigation. **Mats Halvarsson:** Writing – review & editing, Visualization, Validation, Supervision, Resources, Project administration, Methodology, Funding acquisition, Conceptualization.

Declaration of competing interest

The authors declare the following financial interests/personal relationships which may be considered as potential competing interests:

Dirk Stiens, Wiebke Janssen and Johannes Kümmel are employees or former employees of Walter AG, a commercial cutting tool manufacturer, which may be considered as potential competing interest. If there are other authors, they declare that they have no known competing financial interests or personal relationships that could have appeared to influence the work reported in this paper.

Data availability

Data will be made available on request.

Acknowledgements

This work is part of the CVD 2.0 project, supported by the Swedish Foundation for Strategic Research (SSF). This research was mainly carried out at the Chalmers Materials Analysis Laboratory (CMAL). The authors want to thank Dr. Antiope Lotsari from the Department of Chemistry, Chalmers University of Technology, for fruitful discussions about defects.

References

[1] S. Ruppi, B. Högrelius, M. Huhtiranta, Wear characteristics of TiC, Ti(C,N), TiN and A12O3 coatings in the turning of conventional and Ca-treated steels, Int. J. Refract. Met. Hard Mater. 16 (1998) 353–368, https://doi.org/10.1016/S0263-4368(98)00039-0.

[2] L. Karlsson, L. Hultman, M.P. Johansson, J.E. Sundgren, H. Ljungcrantz, Growth, microstructure, and mechanical properties of arc evaporated TiCxN1-x (0≤x≤1) films, Surf. Coat. Technol. 126 (2000) 1–14, https://doi.org/10.1016/S0257-8972(00)00518-1.

[3] H. Hyakutake, Y. Imada, F. Honda, K. Nakajima, Mechanical properties of TiN-TiC mixed crystal films, J. Phys. Condens. Matter 10 (1998) 111–121, https://doi.org/10.1088/0953-8984/10/1/013.

[4] R.S. Bonetti, H. Wiprächtiger, E. Mohn, CVD of titanium carbonitride at moderate temperature: properties and applications, Met. Powder Rep. 45 (1990) 837–840, https://doi.org/10.1016/0026-0657(90)90575-2.

[5] A. Paseuth, H. Fukui, S. Okuno, H. Kanaoka, Y. Okada, Microstructure, mechanical properties, and cutting performance of TiCxN1-x coatings with various x values fabricated by moderate temperature chemical vapor deposition, Surf. Coat. Technol. 260 (2014) 139–147, https://doi.org/10.1016/j.surfcoat.2014.09.068.

[6] A. Paseuth, H. Fukui, K. Yamagata, Improvement of mechanical properties and cutting performance of modified MT-TiCxN1-x coating by moderate temperature chemical vapor deposition, Surf. Coat. Technol. 291 (2016) 54–61, https://doi.org/10.1016/j.surfcoat.2016.02.023.

[7] C. Kainz, N. Schalk, M. Tkadletz, M. Winkler, C. Czettl, Microstructure, mechanical and thermo-physical properties of CVD TiCxN1-x coatings on cemented carbide substrates grown with C2H6 as C feeding precursor, Surf. Coat. Technol. 394 (2020) 125868, https://doi.org/10.1016/j.surfcoat.2020.125868.

[8] S. Kudapa, K. Narasimhan, P. Boppana, W.C. Russell, Characterization and properties of MTCVD TiCN and MTCVD ZrCN coatings, Surf. Coat. Technol. 120–121 (1999) 259–264, https://doi.org/10.1016/S0257-8972(99)00484-3.

[9] H. Holzschuh, Chemical-vapor deposition of wear resistant hard coatings in the Ti-B-C-N system: properties and metal-cutting tests, Int. J. Refract. Met. Hard Mater. 20 (2002) 143–149, https://doi.org/10.1016/S0263-4368(02)00013-6.

[10] S. Ruppi, A. Larsson, Deposition, microstructure, and properties of nanocrystalline Ti(C,O,N) coatings, J. Vac. Sci. Technol. A: Vac. Surf. Films 21 (2003) 66–75, https://doi.org/10.1116/1.1521965.

[11] C. Czettl, C. Mitterer, U. Mühle, D. Rafaja, S. Puchner, H. Hutter, M. Penoy, C. Michotte, M. Kathrein, CO addition in low-pressure chemical vapour deposition of medium-temperature TiCxN1-x based hard coatings, Surf. Coat. Technol. 206 (2011) 1691–1697, https://doi.org/10.1016/j.surfcoat.2011.07.086.

[12] A. Larsson, S. Ruppi, Microstructure and properties of Ti(C,N) coatings produced by moderate temperature chemical vapour deposition, Thin Solid Films 402 (2002) 203–210, https://doi.org/10.1016/S0040-6090(01)01712-6.

[13] L. von Fieandt, K. Johansson, T. Larsson, M. Boman, E. Lindahl, On the growth, orientation and hardness of chemical vapor deposited Ti(C,N), Thin Solid Films 645 (2018) 19–26, https://doi.org/10.1016/j.tsf.2017.10.037.

[14] L. von Fieandt, T. Larsson, M. Boman, E. Lindahl, Texture formation in chemical vapor deposition of Ti(C,N), J. Cryst. Growth 508 (2019) 90–95, https://doi.org/10.1016/j.jcrysgro.2018.12.030.

[15] R. Qiu, S. Shoja, L. von Fieandt, J. Engqvist, O. Bäcke, H.O. Andrén, M. Halvarsson, Schmid factor analysis for chip flow induced plastic deformation of textured cubic carbonitride coatings, Int. J. Refract. Met. Hard Mater. 108 (2022), https://doi.org/10.1016/j.ijrmhm.2022.105932.

[16] J. Garcia, R. Pitonak, R. Weißenbacher, A. Köpf, F. Soldera, S. Suarez, F. Miguel, H. Pinto, A. Kostka, F. Mücklich, Design and characterization of novel wear resistant multilayer CVD coatings with improved adhesion between Al2O3 and Ti(C,N), Adv. Eng. Mater. 12 (2010) 929–934, https://doi.org/10.1002/adem.201000130.

[17] N. Schalk, M. Tkadletz, C. Mitterer, Hard coatings for cutting applications: physical vs. chemical vapor deposition and future challenges for the coatings community, Surf. Coat. Technol. 429 (2022) 127949, https://doi.org/10.1016/j.surfcoat.2021.127949.

[18] I. Endler, M. Höhn, M. Herrmann, R. Pitonak, S. Ruppi, M. Schneider, H. van den Berg, H. Westphal, Novel aluminum-rich Ti1-xAlxN coatings by LPCVD, Surf. Coat. Technol. 203 (2008) 530–533, https://doi.org/10.1016/j.surfcoat.2008.04.098.

[19] M. Ben Hassine, H.O. Andrén, A.H.S. Iyer, A. Lotsari, O. Bäcke, D. Stiens, W. Janssen, T. Manns, J. Kümmel, M. Halvarsson, Growth model for high-Al containing CVD TiAlN coatings on cemented carbides using intermediate layers of TiN, Surf. Coat. Technol. 421 (2021), https://doi.org/10.1016/j.surfcoat.2021.127361.

[20] R. Qiu, O. Bäcke, D. Stiens, W. Janssen, J. Kümmel, T. Manns, H.O. Andrén, M. Halvarsson, CVD TiAlN coatings with tunable nanolamella architectures, Surf. Coat. Technol. 413 (2021) 127076, https://doi.org/10.1016/j.surfcoat.2021.127076.

[21] R. Qiu, L. von Fieandt, J. Engqvist, D. Stiens, O. Bäcke, H.O. Andrén, M. Halvarsson, Facet identification in textured polycrystalline coatings by EBSD-aided SEM trace analysis, Mater. Charact. 209 (2024), https://doi.org/10.1016/j.matchar.2024.113743.

[22] S.J. Pennycook, Z-contrast stem for materials science, Ultramicroscopy 30 (1989) 58–69, https://doi.org/10.1016/0304-3991(89)90173-3.
[23] M. Zhu, S. Achache, P. Boulet, A. Virfeu, J.F. Pierson, F. Sanchette, Effects of deposition parameters on the microstructure and mechanical properties of Ti(C,N) produced by moderate temperature chemical vapor deposition (MT-CVD) on cemented carbides, Vacuum 195 (2022), https://doi.org/10.1016/j.vacuum.2021.110650.
[24] L. Qiu, Y. Du, Z. Zhong, H. Shi, L. Albir, Influence of annealing on the microstructure and mechanical properties of MTCVD TiC0.79N0.21 coating, Vacuum 148 (2018) 88–97, https://doi.org/10.1016/j.vacuum.2017.10.040.